

## Uncovering the primary X-ray emission and possible starburst component in the polarized NLS1 Mrk 1239

MARGARET Z. BUHARIWALLA,<sup>1</sup> SOPHIA G. H. WADDELL,<sup>1</sup> LUIGI C. GALLO,<sup>1</sup> DIRK GRUPE,<sup>2</sup> AND S. KOMOSSA<sup>3</sup>

<sup>1</sup>*Department of Astronomy & Physics, Saint Mary's University, 923 Robie Street, Halifax, Nova Scotia, B3H 3C3, Canada*

<sup>2</sup>*Dept. of Physics, Earth Science, and Space System Engineering, Morehead State University, 235 Martindale DR, Morehead, KY 40351, USA*

<sup>3</sup>*Max-Planck-Institut für Radioastronomie, Auf dem Hügel 69, 53121, Bonn Germany*

(Received xxx yyy zzz; Revised xxx yyy zzz; Accepted Aug 17 2020)

Submitted to ApJ

### ABSTRACT

X-ray observations of the unique NLS1 galaxy Mrk 1239 spanning 18-years are presented. Data from *XMM-Newton*, *Suzaku*, *Swift* and *NuSTAR* are combined to obtain a broad-band, multi-epoch view of the source. There is spectral variability in the 3 – 10 keV band over the 18-years. An analysis of the *NuSTAR* and *Suzaku* light curves also suggests rapid variability in the 3 – 10 keV band, which is consistent with the NLS1 definition of the source. However, no variability is seen below 3 keV on any timescale. Two distinct physical models are adopted to describe the data above and below  $\sim 3$  keV. The low energies are dominated by a hot, diffuse gas likely associated with a starburst component at large physical scales. The higher energy spectrum is dominated by emission from the central region. Ionised partial covering and relativistic blurred reflection are considered for the central region emission. In both cases, the underlying power law has a photon index of  $\Gamma \sim 2.3 - 2.4$ . A distant reflector, a neutral partial covering component with a covering fraction near  $\sim 1$ , and contributions from starburst emission are always required. The blurred reflection model requires a reflection dominated spectrum, which may be at odds with the low emissivity index and radio properties of the source. By contrast, the two absorption components required in the ionised partial covering model may correspond to the two distinct regions of polarization observed in the optical. Regardless of the physical model, spectral changes between epochs are driven by the absorption components and on short time scales by intrinsic AGN variability.

**Keywords:** galaxies: active – galaxies: nuclei – galaxies: individual: Mrk 1239 – X-rays: galaxies

### 1. INTRODUCTION

Active Galactic Nuclei (AGN) are powered by supermassive black holes which are accreting material from their surroundings. AGN emit light across the entire electromagnetic spectrum and are typically variable at all wavelengths. Studying the X-ray emission from these objects allows for the characterisation of the innermost regions of the system, where extreme relativistic effects occur.

AGN are typically classified based on their viewing angle, where Seyfert 1 (type-1) AGN provide a direct view of the central engine, and Seyfert 2 (type-2) AGN are viewed through the cold, obscuring torus (Antonucci 1993). Seyfert 1 galaxies can then be further classified based on their optical properties, in particular, the full-width-half-maximum

(FWHM) of the H $\beta$  line. Narrow-line Seyfert 1 (NLS1) galaxies have FWHM less than  $2000 \text{ km s}^{-1}$ , while broad-line Seyfert 1 (BLS1) galaxies have FWHM greater than  $2000 \text{ km s}^{-1}$  (Osterbrock & Pogge 1985; Goodrich 1989). The narrower lines observed in NLS1s are typically explained by lower mass AGN which are accreting at a higher fraction of their Eddington limit (Pounds et al. 1995; Grupe et al. 2004; Komossa 2008).

The X-ray spectra of type-1 AGN is dominated by a power law. The origin of the power law is the X-ray emitting corona, a source of hot electrons located at some height above the black hole. UV seed photons from the accretion disc are Compton up-scattered in the corona and re-emitted as X-rays in the form of a power law. Many spectra also show evidence of a prominent emission line at  $\sim 6.4$  keV. This is typically attributed to Fe K $\alpha$  emission from neutral iron, originating in the torus, a distant cloud of neutral gas and dust (e.g. Nandra et al. 2007). Above 10 keV, spectra show

evidence for a Compton hump, peaking at 20 – 30 keV. This feature is produced via Compton down-scattering of photons from the corona in an optically thick medium, such as the torus or the accretion disc.

Below  $\sim 2$  keV, many Seyfert 1 AGN show a strong soft excess of disputed origin. This feature has been shown to be particularly prominent in NLS1 galaxies (e.g. [Boller et al. 1996](#); [Grupe et al. 1998](#); [Puchnarewicz et al. 1992](#)). One commonly adopted interpretation is the partial covering scenario, wherein the soft excess is produced via absorption of X-rays from the corona (e.g. [Tanaka et al. 2004](#)). The absorber is typically located close to the corona, and a number of ionisation states, densities, and covering fractions of the absorbing material can be adopted to explain the observed emission. This interpretation has been used to model the observed spectra of numerous type-1 AGN (e.g. [Miyakawa et al. 2012](#); [Gallo et al. 2015](#)).

An alternative interpretation is known as the blurred reflection scenario (e.g. [Ross & Fabian 2005](#)). In this model, some fraction of photons emitted by the corona are incident upon the accretion disc. As the photons interact with the disc, they produce strong emission and absorption features, most of which are associated with iron and have energies below  $\sim 2$  keV. As the disc rotates, the material is subject to extreme general relativistic effects, and the features appear broadened. This produces a strong soft excess, as well as a broadened Fe K $\alpha$  line between 4 – 7 keV. This model has been successfully applied to the spectra of numerous NLS1 galaxies ([Fabian et al. 2004](#); [Ponti et al. 2010](#); [Gallo et al. 2019](#)).

When the continuum (power law) component is significantly suppressed, for whatever reason, the underlying components can often be distinguished. In dim sources, distant reflection from the torus and even X-ray emission from star formation in the galaxy can also contribute to the soft excess (e.g. [Franceschini et al. 2003](#); [Gallo et al. 2019](#); [Parker et al. 2019](#)). While the partial covering and blurred reflections typically produce smoother soft excesses, the torus and star formation regions lie far away from the central engine and are not subject to extreme relativistic effects. The emission and absorption features therefore appear narrow.

Mrk 1239 (RX J0952.3-0136) is typically classified as a NLS1 galaxy and is found at a redshift of  $z = 0.01993$  ([Beers et al. 1995](#)). The source has been studied at many wavelengths and numerous interesting properties have been revealed. The mass of the supermassive black hole at the centre of Mrk 1239 has been reported as  $2.4 \times 10^6 M_{\odot}$  ([Marin 2016](#)). [Véron-Cetty & Véron \(2001\)](#) measure a FWHM of  $1075 \text{ km s}^{-1}$  for the H $\beta$  line, moderate [O III] emission strength ([O III]/H $\beta$  = 1.29), and weak Fe II emission ([Fe II]/H $\beta$  = 0.63). Additionally, the optical spectrum shows evidence for polarisation on the order of  $\sim 3 - 4\%$ , and has

one of the highest degrees of polarisation reported in [Martin et al. \(1983\)](#). [Goodrich \(1989\)](#) show that the Balmer lines and forbidden optical lines show different degrees of polarisation and suggest that these features have distinct physical origins, polarised due to dust reflection and transmission.

In the radio regime, Mrk 1239 has been classified as both radio-quiet ([Doi et al. 2015](#)), or borderline radio-loud ([Berton et al. 2018](#)). [Doi et al. \(2015\)](#) show that the radio emission cannot solely be attributed to starburst activity and must also comprise AGN jet activity. They classify this source as a Fanaroff-Riley Type I candidate ([Fanaroff & Riley 1974](#)), meaning that the radio luminosity decreases with increasing distance from the centre of the galaxy. [Doi et al. \(2015\)](#) also give clear evidence for kilo-parsec scale non-thermal radio emission attributed to AGN jets, however, most of the radio power is centred in the inner 100 pc.

Based on near-infrared observations, Mrk 1239 has some evidence for star forming regions based on signatures from polycyclic aromatic hydrocarbon (PAH). [Ruschel-Dutra et al. \(2016\)](#) and [Jensen et al. \(2017\)](#) both report signatures of PAH at  $11.3 \mu\text{m}$ , although both suggest that these features do not lie in the inner nucleus, but rather a few hundred pc from the centre. [Rodríguez-Ardila & Viegas \(2003\)](#) place only an upper limit on a  $3.3 \mu\text{m}$  PAH detection, also state that starburst activity may be occurring a few hundred pc from the nucleus. An estimated star formation rate (SFR) of less than  $7.5 M_{\odot} \text{ yr}^{-1}$  ([Ruschel-Dutra et al. 2016](#)) has been measured. [Sani et al. \(2010\)](#) find that Mrk 1239 exhibits weaker star formation relative to AGN emission than the average NLS1. As well, [Rodríguez-Ardila & Mazzalay \(2006\)](#) reported a remarkable NIR bump, they interpret it as a massive reservoir of dusty gas between NLR and BLR. This could explain strong continuum absorption.

In the X-ray, observations with *ROSAT* and *XMM-Newton* have previously been analysed. [Rush & Malkan \(1996\)](#) report a soft X-ray slope of  $\Gamma \simeq 3$  using *ROSAT* and find absorption higher than the Galactic  $N_{\text{H}}$  value by a factor of  $\sim 1.5$ . Mrk 1239 is also included in the *ROSAT* sample analysed by [Boller et al. \(1996\)](#), where a steep soft X-ray slope of 3.9 and a high column density of  $8.3 \times 10^{20} \text{ cm}^{-2}$  is reported. [Grupe et al. \(2004\)](#) report on a 10 ks *XMM-Newton* observation of Mrk 1239, using data from the EPIC-pn and MOS detectors. They find that the spectral shape can successfully be reproduced using a power law which is almost entirely absorbed by two distinct absorbers, akin to the two polarisation regions reported in [Goodrich \(1989\)](#). They also report a strong feature around 0.9 keV found in all three detectors, which they attribute to a strong Ne IX line due to a super-solar Ne/O ratio ([Grupe et al. 2004](#)).

This work presents the spectral and timing analysis of all available X-ray data from *XMM-Newton*, *Suzaku*, *NuSTAR* and *Swift*, spanning 18 years between 2001 and 2019, and

seeks to explain the unique X-ray properties of the source. In Section 2, the observations and data reduction techniques are summarised. Section 3 examines the variability of the source across both long (years) and short (hours) timescales and in Section 4 the spectra are analyzed. A discussion of the results is given in Section 5, and conclusions are drawn in Section 6.

## 2. OBSERVATIONS AND DATA REDUCTION

Mrk 1239 was observed with *XMM-Newton*, *Suzaku*, and *NuSTAR/Swift* at three different epochs over 18 years. The data analysed here are listed in Table 1. This section describes the observations and data reduction.

### 2.1. *XMM-Newton*

Mrk 1239 was observed with *XMM-Newton* (Jansen et al. 2001) for  $\sim 10$  ks in late 2001. The source appears in the field of view of the target source, RXJ 095208.7-014818, and is therefore substantially off axis.

The *XMM-Newton* Observation Data Files (ODF) were processed to produce a calibrated event list using the *XMM-Newton* Science Analysis System, SAS v17.0.0. Examination of the background showed significant flaring in the EPIC-pn detector. A good time interval (GTI) was created and applied. Background flaring was not significant in the EPIC-MOS1 and MOS2 detectors.

For each detector, source photons were extracted from a circular region with a  $35''$  radius centred on Mrk 1239, and background photons were extracted from an off-source circular region with a  $50''$  radius on the same CCD. For the pn detector, single and double events were selected, while single to quadruple events were selected for the MOS detectors. The SAS tasks RMFGEN and ARFGEN were used to generate response files. *XMM-Newton* light curves were not examined due to the short length of the observation (10 ks).

The source and background spectra were binned with a minimum of 10 counts per bin. The final pn, MOS1 and MOS2 spectra were checked for consistency, and all spectra were found to be comparable within known uncertainties.<sup>1</sup> The pn spectrum had low counts due to background flare filtering and the source was located at the very edge of the detector. For this reason, the combined MOS data are used for further analysis. The ungrouped MOS1 and MOS2 source and background spectra were merged using ADDSPEC, and the corresponding response files merged using ADDRMF and ADDARF. The combined source and background spectra were then binned with a minimum of 10 counts per bin. This combined MOS spectrum had a higher signal and lower background than the pn detector, allowing for improved spec-

tral modelling. Data above 8 keV are background dominated so only the 0.3 – 8 keV range is used for spectral modelling.

### 2.2. *Suzaku*

Mrk 1239 was the target of a  $\sim 126$  ks *Suzaku* (Mitsuda et al. 2007) observation in May 2007. The data were taken in XIS nominal mode. Extraction of spectra and light curves was performed with XSELECT v2.4G using cleaned event files from the front illuminated (FI; XIS0 and XIS3) and back illuminated (BI; XIS1) CCDs.

For each instrument, source photons were extracted using a  $240''$  region centred around the source, while background photons were extracted from a  $180''$  off-source region, while avoiding the calibration regions in the corners of the CCDs. Response matrices for each detector were generated using the tasks XISRMFGEN and XISSIMARFGEN. Source and background spectra for each detector were then binned using the optimal binning routine in FTGROUPPHA (Kaastra & Bleeker 2016). The XIS spectra were checked for consistency and found to be comparable with one another. The XIS0 and XIS3 source and background spectra were then merged using ADDASCASPEC. For simplicity, only the merged FI spectra are presented for the remainder of the analysis. The XIS spectrum is modelled between 0.7–10 keV, while excluding 1.5 – 2.5 keV due to calibration uncertainties.

Cleaned event files from the HXD-PIN detector were processed using the tool HXDPINXBPI, resulting in a 54 ks exposure. Both the non-X-ray background (NXB) and the cosmic X-ray background (CXB) are used to determine the background level. The source is detected at  $\sim 4.5$  per cent between 12–20 keV, which is considered marginal (Fukazawa et al. 2009).

### 2.3. *NuSTAR* and *Swift*

Mrk 1239 is part the *NuSTAR* (Harrison et al. 2013) Extragalactic Legacy Survey, specifically the *NuSTAR* Local AGN NH Distribution Survey (NuLANDS). NuLANDS is designed to look at heavily obscured AGN in the local universe (Boorman et al. 2018). There are 30 AGN in the sample and observations were completed in 2019.

Mrk 1239 was observed in June 2019 with a simultaneous *Swift* observation shortly after *NuSTAR* began. FPMA and FPMB data were extracted from source region of  $75''$ . A background was selected from the same chip with a region of  $115''$ . The data were processed with CALDB index version 20181030. The joint *Swift* XIS spectrum was obtained from the *Swift*-XRT data product generator (Evans et al. 2009)<sup>2</sup>.

The *NuSTAR* data were optimally binned using FTGROUPPHA. The *Swift* spectra were binned to have a minimum of 10 counts per bin using GRPPHA.

<sup>1</sup> <https://xmmweb.esac.esa.int/docs/documents/CAL-TN-0018.pdf>

<sup>2</sup> [www.swift.ac.uk/user\\_objects/](http://www.swift.ac.uk/user_objects/)

(1)	(2)	(3)	(4)	(5)	(6)	(7)	(8)
Observatory	Observation ID	Name	Start Date (yyyy-mm-dd)	Duration [s]	Exposure [s]	Counts	Energy Range [keV]
<i>XMM-Newton</i> MOS 1+2	0065790101	MOS	2001-11-12	9959	9371/9371	1052	0.3-8.0
<i>Suzaku</i> XIS 0+3	702031010	XIS	2007-05-06	126256	63128	6555	0.7-1.5, 2.5-10
<i>Suzaku</i> PIN		PIN		535904		14654	12-20
<i>NuSTAR</i> FPMA/FPMB	60360006002	FPMA/FPMB	2019-06-17	38053	21093	2039/1954	3-30
<i>Swift</i> XRT	00081986001	XRT	2019-06-17	18624	6216	183	0.5-7

**Table 1.** Observations log for Mrk 1239. The observations and instruments used for analysis are listed in column (1). The observation ID and labels used in this work are given in columns (2) and (3), respectively. The start date of each observation is given in column (4). The duration of each observation, total exposure time and total counts for each observation are given in columns (5), (6), and (7), respectively. The energy each observation were fit over is given in column (8). For *Suzaku* the combined counts from XIS0 and XIS3 are given (column 7). Similarly for *XMM-Newton* the combined counts from MOS1 and MOS2 is reported.

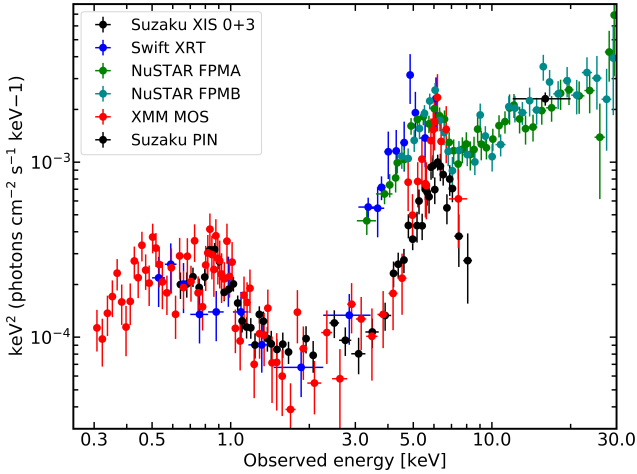


**Figure 1.** The unfolded spectra of Mrk 1239, with observations spanning 18 years. Data from *XMM-Newton* are shown in red, *Suzaku* are shown in black, *NuSTAR* are shown in green and aqua, and *Swift* are shown in blue. The data are compared to a flat power law with  $\Gamma = 0$ . The intrinsic spectrum is hard, and spectral changes are apparent in the 3 – 10 keV band.

### 3. CHARACTERIZING THE VARIABILITY

#### 3.1. Long term Variability

The unfolded spectra of Mrk 1239 compared to a flat ( $\Gamma = 0$ ) power law are plotted in Figure 1. Plotting the unfolded spectra in this way allows us to directly compare data from different instruments, highlighting any spectral differences at each of the three epochs.

The soft band (0.3 – 3 keV) is remarkably similar between epochs, displaying the same flux and curved spectral shape in the XRT, XIS and MOS spectra. The large hump like feature appears to be a soft excess. This feature has been consistently observed in this source outside the observations included in this paper. The source was also observed using *ROSAT* (Truemper 1982) in 1992. Rush & Malkan (1996) fit the source with an absorbed power law and found that was an acceptable fit. However the fit was improved using an

additional component, either thermal emission (black body or Raymond-Smith thermal plasma) or an emission line at  $\sim 0.7$  keV. The spectra lacked the data quality to distinguish between any of the models. An emission line-like feature at  $\sim 0.9$  keV was also reported by Grupe et al. (2004) in the EPIC-pn spectra. This feature is prevalent in all the data.

The most significant variability appears between 3 – 10 keV. The flux and spectral shape of the source is different in 2019 compared to the earlier XIS and MOS observations. In particular, the *NuSTAR* and *Swift* data are a factor of  $\sim 2 - 3$  brighter than the XIS and MOS data in this energy range. The MOS and XIS data are remarkably similar across the entire energy range. There is a slight discrepancy around  $\sim 6 - 7$  keV, where the MOS data appear slightly brighter; however, the spectra remain consistent within error.

The source is significantly detected in *NuSTAR* up to  $\sim 30$  keV. The source is only marginally detected in the PIN, but appears to be comparable in brightness at the two epochs (2007 and 2019). We cannot comment on any change in shape between epochs because the PIN data are limited.

#### 3.2. Rapid variability

Having established that there is some long-term variability in the 3 – 10 keV band, we examine light curves for rapid variability over the course of the *NuSTAR* and *Suzaku* observations. The FPMA and FPMB lightcurves were merged to improve signal-to-noise, as were the XIS0 and XIS3 lightcurves. Variability was examined using 500 s and 5780 s bins, where 5780 s corresponds approximately to the orbital period of the satellites. The lightcurves were binned using LCURVE. Given the modest data quality, all lightcurves and hardness ratios are compared to their mean value to examine variability. The fit quality is given by a reduced  $\chi^2$  test. In Figure 2 and Table 2, the light curves and fits are presented.

The XIS lightcurve for the soft band (0.5 – 3 keV) has a mean count rate of  $\sim 0.05$  count  $s^{-1}$ . The  $\chi^2/dof$  for the light curves is 144/145 using the 500 s bins and 11/21 using



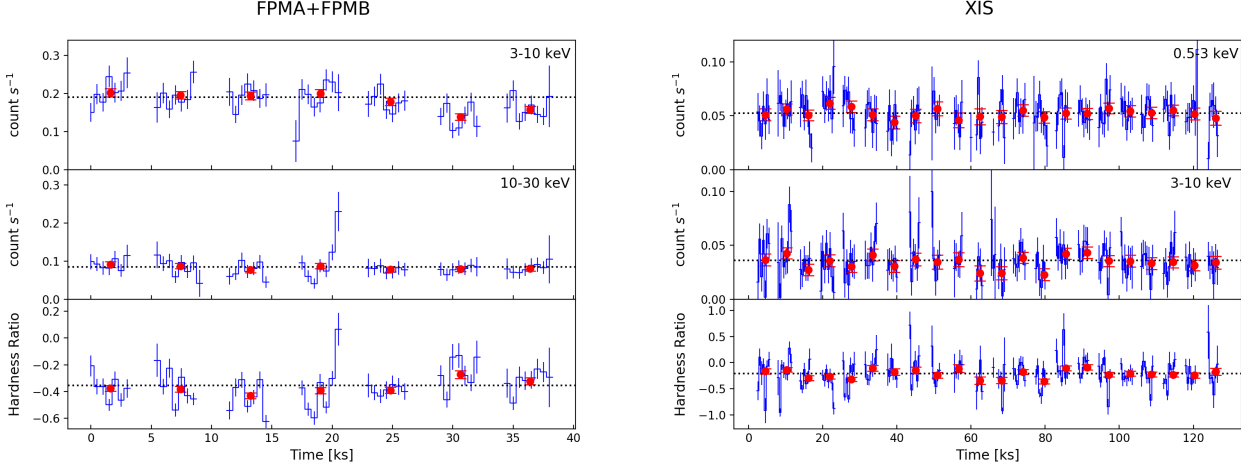


**Figure 2.** *Left:* *NuSTAR* light curve with FPMA and FPMB combined. Top panel is the 3-10 keV band, middle is the 10-30 keV band and bottom panel is the hardness ratio calculated by:  $HR = (H - S)/(H + S)$ . *Right:* *Suzaku* light curve. Top panel is the 0.5-3 keV band, middle is the 3-10 keV band and bottom panel is the hardness ratio. In all panels the dashed line is the average count rate or HR.

(1) Instrument	(2) Energy band	(3) $\chi^2/dof$	
		500 s	5780 s
FPMA+FPMB	3 – 10 keV	101/50	41/6
	10 – 30 keV	53/50	4/6
	HR <sub>FPM</sub>	198/49	25/6
XIS	0.5 – 3 keV	144/145	11/21
	3 – 10 keV	139/142	23/21
	HR <sub>XIS</sub>	658/139	52/21

**Table 2.** The fit statistic for each lightcurve and HR compared to their mean value. Column (1) indicates which instrument the light curve was produced by. Column (2) states the energy bin of the lightcurve. Column (3) gives the fit quality when the mean is fit for each light curve.

the 5780 s bins. This indicates that the source is not variable below 3 keV on short time scales.

The hard band (10 – 30 keV) was only observed with *NuSTAR*, and has a mean count rate of  $\sim 0.1 \text{ count s}^{-1}$ . The  $\chi^2/dof$  of the 500 s and 5780 s bin lightcurves are 53/50 and 4/6, respectively. The slight difference in the  $\chi^2$  values may be the result of a flare in the 500 s bin lightcurve at approximately 20 ks. On short time scales, the hard band remains constant in flux within uncertainties.

The intermediate band (3 – 10 keV) is the only band that has overlap between *NuSTAR* and XIS. In the XIS lightcurve the mean count rate is  $\sim 0.04 \text{ count s}^{-1}$ . The AGN is more significantly detected in *NuSTAR* and the mean count rate is  $\sim 0.2 \text{ count s}^{-1}$ . Upon visual inspection the intermediate

band appears to have more variability compared to the soft and hard bands. This is confirmed in the constant fit test. The *NuSTAR* 500 s and orbital binned light curves are inconsistent with constants and have  $\chi^2/dof = 101/50$  and  $41/6$ , respectively. The XIS data shows marginal variability (23/21) in the orbital binned lightcurve in this band and none in the 500 s bin lightcurve. However due to the low count rate it is difficult to rule out rapid variability in the XIS lightcurves.

The hardness ratio (HR) for the XIS lightcurves, HR<sub>XIS</sub>, has a mean value of  $\sim -0.2$ , indicating that the soft count rate is higher than the intermediate count rate. The *NuSTAR* HR<sub>FPM</sub> has a mean value of  $\sim -0.4$ , indicates the intermediate count rate is higher than the hard count rate. All HR curves are inconsistent with a constant fit ( $\chi^2/dof > 1$ ) indicating a significant amount of spectral variability. This spectral variability is driven by fluctuations in the intermediate, 3 – 10 keV, band. This is the same result found on long time scales (Figure 1). On both time scales there is very little change in the soft band, which remained constant in shape and flux. The intermediate band changes in shape and flux on long time scales, as well it changes in flux on rapid time scales.

The excess variance ( $\sigma_{\text{rms}}^2$ ) (e.g. Ponti et al. 2012) is calculated for the *NuSTAR* 3 – 10 keV light curve to further examine the rapid variability. The light curve is binned in 200 s and subdivided in 10 ks segments. The excess variance is calculated in each segment and then averaged over all of the segments. The measured average value for Mrk 1239 during the *NuSTAR* observation is  $\sigma_{\text{rms}}^2 = 0.04 \pm 0.01$ . The value is comparable to that measured in other NLS1 galaxies (Ponti et al. 2012).

Seyfert 1 AGN can display substantial variability at lower energies, and NLS1s in particular are known to display extreme soft variability on both short and long timescales (e.g.

Boller et al. 1996; Leighly 1999; Grupe et al. 2001; Nikolajuk et al. 2009; Grupe et al. 2010; Komossa et al. 2016; Bonson et al. 2018; Gallo 2018). The differences in the rapid and long term spectral variability may be pointing to different origins for the soft ( $< 3$  keV) and intermediate (3 – 10 keV) emission. This suggests that the primary source of the soft excess is highly atypical compared to other NLS1s. However, the variability above 3 keV seen on both short and long timescales is more typical of what is seen in other sources, implying a distinct origin from the soft excess. More discussion for this will be given in Section 5.

#### 4. SPECTRAL MODELLING

All data were background modelled in XSPEC, except for the PIN data which was background subtracted. We used C-statistics (Cash 1979) to evaluate the fit quality throughout. Errors were calculated at the 90 per cent confidence level using the XSPEC error command. The *NuSTAR* and *Swift* spectra were treated as one epoch for all spectral modelling. All model parameters were linked between them. The same was done for the *Suzaku* XIS and PIN data. A cross-calibration constant was applied to the FPMB detector in *NuSTAR*, the XRT data from *Swift* and the PIN data from *Suzaku*. The constant was free for FPMB and XRT and monitored to ensure it remained within acceptable ranges, as prescribed by *NuSTAR* FAQ<sup>3</sup>. The constant applied to the PIN data was frozen at 1.18<sup>4</sup>. A Galactic column density of  $N_{\text{H}} = 4.43 \times 10^{20}$  (Willingale et al. 2013) was applied to all models and frozen throughout spectral fitting. Wilms et al. (2000) abundances were used throughout spectral fitting.

Figure 3 shows each spectra separately with its background model, and ratio for an absorbed power law with  $\Gamma = 2$  to represent a typical NLS1. As we can see in Figure 3, all spectra exhibit curvature and none are fit well by the power law. All five spectra show evidence for excess emission between 5 – 8 keV. The MOS spectrum shows a soft excess below 1 keV and all spectra are over estimated by the model in the 2 – 5 keV range.

##### 4.1. *NuSTAR*/*Swift*

We begin by examining only the *NuSTAR* and *Swift* spectra, and only consider data above 2 keV. This is the first time this data set has been examined in detail and it provides the best view of the AGN above 10 keV. The examination of the unfolded spectrum reveals many key characteristics; an underlying power law component, extreme spectral curvature around 3 – 8 keV, and a potential narrow feature at 6.4 keV. To model these features, we apply a power

law plus a cold ( $\log \xi = 0$ ; where the ionisation parameter  $\xi = L/nr^2$  and  $L$  is the incident luminosity,  $n$  is the column density of the cloud, and  $r$  is the distance from the cloud to the illumination source), distant reflector representing reflection off the torus. To reproduce the observed spectral curvature we modify the power law with a single region of neutral absorption. The XSPEC model would appear as:  $\text{CONSTANT} \times \text{TBABS} \times (\text{XILLVER} + \text{ZPCFABS} \times \text{PO})$ . The constant is the cross calibration constant between FPMA and FPMB and *Swift*. This model was found to provide a suitable fit to the *NuSTAR* / *Swift* data in the 2 – 30 keV band, and gives a fit statistic of  $C/\text{dof} = 356.46/314$ .

We extended the model and data down to 0.5 keV to see if this model is also capable of explaining the spectrum at low energies. This results in a much poorer fit ( $C/\text{dof} = 449.86/338$ ) and a large excess below approximately 1 keV. The addition of a second neutral partial covering component does not improve the fit quality, however the addition of an ionized partial covering absorber (ZXIPCF; Reeves et al. 2008) significantly improves the fit quality ( $C/\text{dof} = 324.03/335$ ). Despite the large change in the C-statistic, there remain significant residuals at approximately 1 keV, as were noted by Grupe et al. (2004). Additionally, all model fits give very high values of the absorber covering fraction ( $CF \sim 0.95 - 1$ ). It therefore seems possible that the intrinsic emission from the AGN is largely obscured below  $\sim 3$  keV, and appears only at high energies.

Based on the work of Ruschel-Dutra et al. (2016) in the mid-infrared, we can infer the existence of star forming regions in Mrk 1239 (see Section 1). Given the lack of evidence for variability at low energies, it is possible that the soft emission does not originate close to the central engine, but rather from star formation on extended scales. We therefore use MEKAL (Liedahl et al. 1995), collisionally ionised emission from hot diffuse gas, to model the SFR. We specify that MEKAL use abundances given by Wilms et al. (2000), with abundance frozen for all spectral fits. This improves the fit to  $C/\text{dof} = 307.92/333$ , and removes the residuals at 1 keV. The measured temperature is  $kT \approx 1$  keV.

Alternatively, we examine if the curvature and hard X-ray emission could be attributed to blurred reflection (eg. Ross & Fabian 2005) rather than the ionized partial covering. By removing the ionized absorber and replacing it with a blurred reflection (RELXILL, García et al. 2014) one gets an acceptable fit with a simple blurred reflection model. A neutral partial covering component and MEKAL are still needed. Furthermore, the use of *NuSTAR* and *Swift* spectra alone does not allow for the constraint of many of the blurred reflection parameters. This model will be explored in more detail using additional data in Section 4.2.2.

##### 4.2. Multi-epoch Spectral Modelling

<sup>3</sup> [https://heasarc.gsfc.nasa.gov/docs/nustar/nustar\\_faq.html](https://heasarc.gsfc.nasa.gov/docs/nustar/nustar_faq.html)

<sup>4</sup> <https://heasarc.gsfc.nasa.gov/docs/suzaku/analysis/abc/node8.html> (See Sec. 5.7.2)

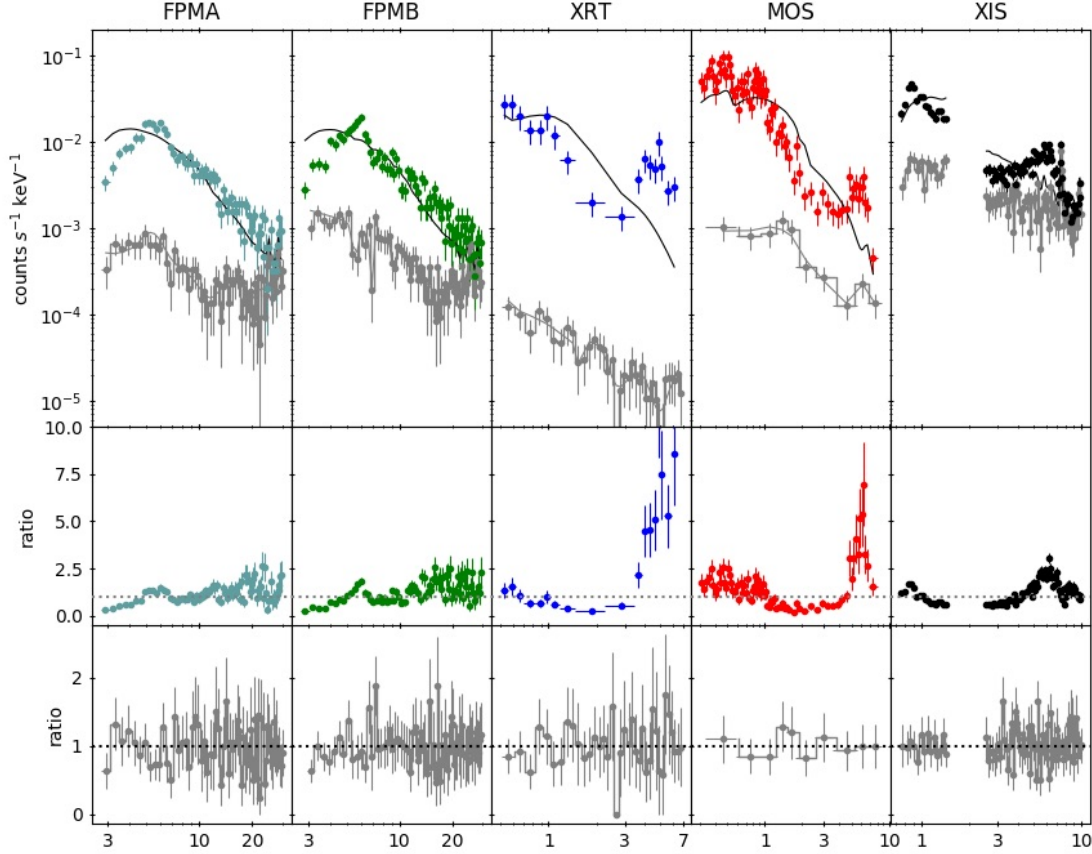


**Figure 3.** *Top row:* The folded source spectra for each instrument with the background shown in grey. The model applied is a power law with Galactic absorption, with  $\Gamma = 2$  and the normalization free for all instruments. This model was applied to emphasize the need for more complex models than a simple power law. *Middle Row:* The ratio of the data with the simple power law model. Comparison to the dotted line at ratio = 1 demonstrates the curvature in the data. *Bottom Row:* The ratio of the background to the background model, with ratio = 1.

In this section, we attempt to describe the behaviour of Mrk 1239 in a self consistent manner using the multi-epoch spectral data collected over 18 years. This has the advantage of giving us low energy sensitivity, provided by MOS and XIS, for the soft excess and the Fe  $K\alpha$  region. *NuSTAR* provides us with good energy coverage up to 30 keV, with simultaneous coverage between 0.5 and 7 keV from *Swift*. This allows us to simultaneously study the soft excess, Fe K region and the broad band continuum. We motivate the models used based on spectral features and variability on multiple time scales.

Structure around the neutral Fe  $K\alpha$  band seen in all spectra are suggestive of distant cold reflection, likely originating in the torus. For this we use XILLVER with  $\log \xi = 0$  to represent a cold reflector.

Study of the long term and rapid variability shows that there is negligible variability below 3 keV. This indicates that direct AGN continuum emission may be highly absorbed

and thus not visible. There is structure seen in the MOS and XIS spectra that may be from distant optically-thin emission from star formation activity. We use MEKAL for this feature.

It also seems possible that the direct AGN component is revealed in the 3-10 keV band, but completely obscured below  $\sim 3$  keV. This indicates the presence of a partial covering absorber (ZPCFABS). We expand upon Section 4.1 by applying the ionized partial covering model and the blurred reflection model to all epochs. Some intrinsic properties of the system were linked, as they are not expected to change on timescales of years. This included the MEKAL component (both normalization and kT), the distant cold reflector (XILLVER) and some of the blurred reflection parameters discussed in detail in Section 4.2.2.

Upon analysis of Figure 1 and fitting both models it was found that the *Suzaku* spectra closely followed the MOS spectra. Linking all parameters between *Suzaku* and MOS

did not significantly decrease the fit quality for either physical model, so they are linked throughout the remainder of the analysis. Allowing for a free constant between the *XMM-Newton* and *Suzaku* models is not a significant improvement to the fit ( $\Delta C = 3$  for one additional free parameter). This leaves us with two epochs; a historic one containing *XMM-Newton* MOS, *Suzaku* XIS and PIN data, and a recent one containing the *NuSTAR* FPMA and FPMB and *Swift* XRT data.

#### 4.2.1. Partial Covering

In a partial covering scenario a cloud of absorbing material with column density ( $N_H$ ) is positioned in the line of sight of the AGN, obscuring a fraction of the direct emission. The model has some fraction of its source emission absorbed and the rest is considered direct emission (e.g. Holt et al. 1980; Tanaka et al. 2004). The model includes three parameters: the column density ( $N_H$ ); the covering fraction (CF), which is the fraction of intrinsic emission that is absorbed; and the redshift ( $z$ ), which remains fixed at  $z = 0.01993$ . The direct emission can be either scattered off the clouds or let through patches in the absorbing material (Tanaka et al. 2004). The patchy absorber is often called a “leaky absorber” (Tanaka et al. 2003) as the direct emission photons can “leak” through the absorber.

Partial covering is often employed to fit NLS1s (e.g. Boller et al. (2002); Tanaka et al. 2005; Turner et al. 2007; Gallo et al. 2015; Iso et al. 2016; Grupe et al. 2019). For Mrk 1239, Grupe et al. (2004) use two absorbing components to model a leaky absorber with the EPIC-pn spectrum. A variation of partial covering is ionized partial covering, where the absorbing medium has some ionization. In this scenario the illumination source is the power law corona (e.g. Reeves et al. 2008).

We adopt a partial covering scenario assuming the absorbers are in a compact region and only the primary continuum (power law) source is absorbed. We include two absorbers, one that is neutral and one with some non-zero ionisation parameter. This is not necessarily two distinct absorbers, but could be representative of a ionisation and density gradient within one medium. The XSPEC model reads: `CONSTANT×TBABS(MEKAL + XILLVER + ZXIPCF×ZPCFABS×POWERLAW)`.

Three scenarios were tested to explain the variability between epochs: (i) constant power law and varying absorbers; (ii) constant absorbers and vary power law; and (iii) absorbers and power law free to vary. The continuum parameters were  $\Gamma$  and the power law normalization. The absorber parameters were both covering fractions (CF), both column densities ( $N_H$ ) and the cloud ionization ( $\log \xi$ ).

The initial model, with all parameters linked between epochs renders a very poor fit ( $C/\text{dof} = 1563.29/603$ ), and

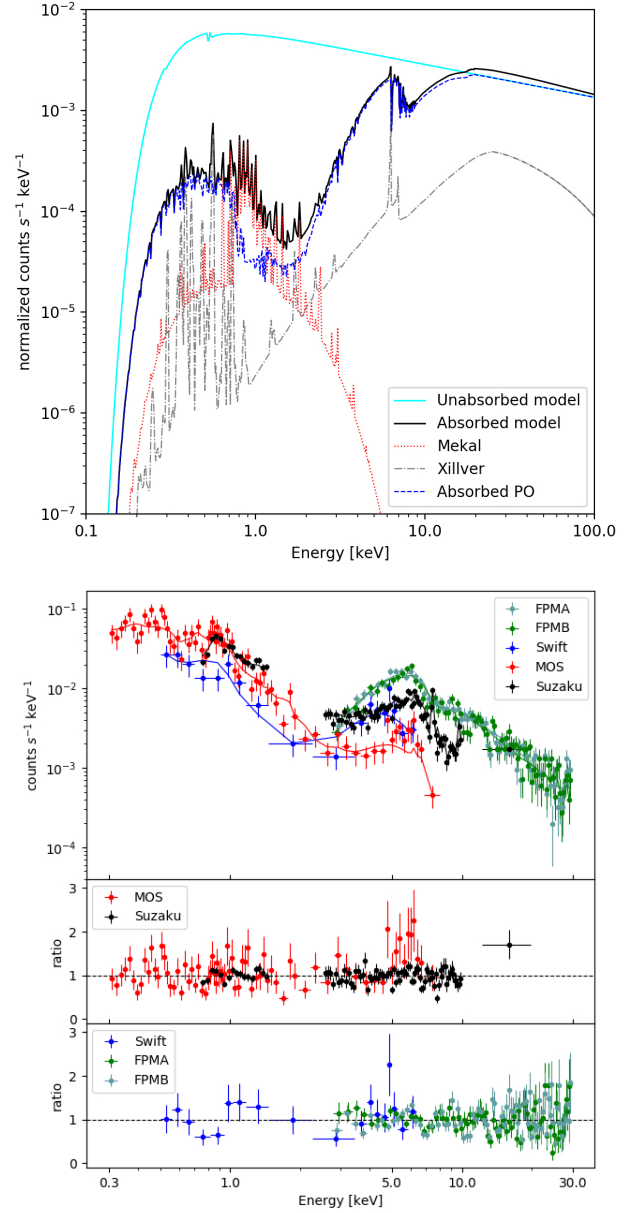


**Figure 4.** *Upper panel:* The theoretical best-fit ionised partial covering model shown over the entire X-ray band. The cyan line shows the continuum power law component with only Galactic absorption applied. *Upper middle panel:* The folded spectra with the best fit partial cover model applied. *Lower middle panel:* The ratio of data to model for the historic epoch, which includes the MOS, XIS and PIN spectra. *Lower panel:* The ratio of data to model for the modern epoch, which contains the XRT and FPMA/FPMB spectra.



the cross-calibration constants for FPMB is far too large to be acceptable ( $\approx 1.7$ ). Allowing the absorber parameters free to vary (Test (i)), we obtain a significantly better fit. If the CF is free at each epoch the fit improves by  $\Delta C = 860.28$  for two additional free parameters. If we allow the  $\log \xi$  to be free between epochs as well the fit improves by  $\Delta C = 39.97$  for two additional free parameter. Allowing all absorber parameters to be free between epochs gives the best fit, with  $C/\text{dof} = 645.50/598$ .

Next, we test a variable continuum with a constant absorber (Test (ii)). Allowing just the power law normalization free between epochs (i.e. linked  $\Gamma$ ), the fit quality is  $C/\text{dof} = 850.13/602$ . Alternatively, permitting  $\Gamma$  to be free between epochs and the normalization linked, the fit quality improves by  $\Delta C = 38$ . If both the photon index and normalization are allowed free between epochs the  $C/\text{dof} = 764.24/601$ , an improvement of  $\Delta C = 47.89$  over the previous fit for one additional free parameter.

If all absorber and continuum parameters are allowed to vary between epochs (Test (iii)), the best fit is  $C/\text{dof} = 645.29/596$ , comparable to Test (i), where the power law parameters are linked between epochs and absorber parameters are free to vary. The data and residuals (separated by epoch) can be seen in Figure 4. The best fit parameters can be seen in Table 3. The measured photon index is  $\Gamma \sim 2.3$ . Compared to Grupe et al. (2004), who reported  $\Gamma \approx 4$ , our value of  $\Gamma$  is much more agreeable with other NLS1s. This highlights the advantage of the high-energy sensitivity provided by *NuSTAR*. The covering fractions of the absorbers in both epochs are very high, each approximately 90 per cent covering. This is consistent with the high degree of optical polarization seen in Martin et al. (1983), and is consistent with the CF found in Grupe et al. (2004) of 0.995.

Figure 4 (top panel) shows the results for the best fitting model applied to only the FPMA data set for clarity. A number of interesting features are revealed. The intrinsic power law is shown in cyan, and the absorbed power law is shown in blue. This reveals that a large amount of absorption is required to reproduce the observed spectral curvature using this interpretation. This is sensible, as we measure covering fractions near 1. Given this high level of absorption at low energies, the MEKAL component (shown in red) is clearly visible in the total model (shown in dark blue). In particular, the strong 0.9 keV feature found by Grupe et al. (2004) is likely explained by this collisionally ionised plasma. This 0.9 keV feature is produced primarily by Fe L transitions. Contributions from the torus are shown in gray, and emission features at low energies also contribute to the soft excess.

The second panel of Figure 4 shows the folded spectrum along with the models for each instrument. The colours are the same as those used in Figure 1. The model appears to provide a good fit to the data. This is more evident in the bottom

panels, where the residuals (data/model) are shown. While some excess residuals are present in the 5 – 7 keV band in the MOS data, the model is clearly able to explain the overall shape of the spectra at each epoch. In particular, no clear excess residuals are seen at low energies, suggesting that the starburst model provides a satisfactory fit to the data. Effectively, the long term variability in Mrk 1239 can be explained largely by changes in a partial covering medium and a relatively constant power law. The excess residuals seen in the MOS data could be due in part to a poor fit of a blurred Fe K $\alpha$  line suggesting a blurred reflection model must be examined.

#### 4.2.2. Blurred Reflection

While there is a high degree of absorption in Mrk 1239, the variability in the 3–10 keV band suggests we may be probing emission from the inner black hole region. Consequently, we examine if it is possible to model the intrinsic emission with a combination of power law and blurred reflection as has been done in some other highly absorbed, type II systems (e.g. Walton et al. 2019).

In blurred reflection, photons emitted by the corona are then incident on the accretion disk where they are absorbed and re-emitted via fluorescence (e.g. Ballantyne et al. 2001; Ross & Fabian 2005). This reflected spectra is then subject to the general relativistic effects that are at play in accretion discs near black holes (e.g. Miniutti & Fabian 2004). Blurred reflection has been successful in describing the spectral and timing properties NLS1s (e.g. Fabian et al. 2009; Chiang et al. 2015; Gallo et al. 2012, Gallo et al. 2015; Jiang et al. 2019; Waddell et al. 2019).

Here, the blurred reflection model, RELXILL (García et al. 2014), replaces the ionized absorber in the partial covering scenario above. Given the data quality, the initial approach is rather conservative. The illumination as a function of distance ( $r$ ) on the disc (emissivity profile) is described by a power law ( $\propto r^{-q}$ ) with index  $q$ . For simplicity,  $q = 3$ , implying the primary emitter is radiating isotropically. The cut off energy ( $E_{\text{cut}}$ ) is frozen at 300 keV, as Mrk 1239 shows no evidence for a high energy cut off. The photon index is linked to the index of the primary power law component. The inner radius is fixed at the inner most stable orbit (ISCO) and the outer radius is fixed at  $400r_g$ . The dimensionless spin parameter defined by  $a = cJ/GM^2$  where  $M$  is the black hole mass and  $J$  is the angular momentum can take on values of 0 (non spinning) to 0.998 (maximum spin). The spin is linked between epochs and initially frozen at 0.998, given the complexities in measuring this parameter (e.g. Bonson & Gallo 2016). The inclination is linked with that of XILLVER, which describes the cold distant reflector (i.e. torus). It is linked between epochs, but left free to vary. The disc ionization pa-

(1) Model	(2) Model Component	(3) Model Parameter	(4) <i>Swift/ NuSTAR</i>	(5) <i>MOS/ Suzaku</i>
Ionized Partial Covering	Ionized absorber ZXIPCF	nH ( $10^{22} \text{ cm}^{-2}$ )	$64^{+37}_{-16}$	$114^{+31}_{-56}$
		$\log \xi$ [ergs cm s $^{-1}$ ]	$2.8^{+0.1}_{-0.2}$	$2.7^{+0.2}_{-0.4}$
		CF	$> 0.86$	$0.9 \pm 0.1$
	Neutral absorber ZPCFABS	nH ( $10^{22} \text{ cm}^{-2}$ )	$13^{+10}_{-7}$	$60^{+19}_{-17}$
		CF	$0.96^{+0.03}_{-0.04}$	$0.89^{+0.04}_{-0.10}$
	Intrinsic	$\Gamma$	$2.3^{+0.3}_{-0.1}$	$2.32 \pm 0.13$
	Power Law	norm <sup>p</sup> ( $10^{-3}$ )	$6^{+4}_{-1}$	$5^{+4}_{-3}$
	FPMB Calibration	constant	$1.00 \pm 0.06$	
	Swift Calibration	constant	$1.0 \pm 0.2$	
	Collisionally Ionized material MEKAL	kT [keV]	-	$0.66 \pm 0.03$
		norm ( $10^{-4}$ ) [cm $^{-5}$ ]	-	$1.3 \pm 0.1$
		Metal Abundance [cosmic]	$1^f$	
	Distant Cold Reflector XILLVER	norm ( $10^{-5}$ )	-	$1.6 \pm 0.6$
		A <sub>Fe</sub> [solar]	$1^f$	
		$\log \xi$ [ergs cm s $^{-1}$ ]	$0^f$	
		E <sub>cut</sub> [keV]	$300^f$	
		Inclination [ $^\circ$ ]	$30^f$	
Unabsorbed Flux	(0.1-100 keV)	$10^{-11}$ [ergs cm $^{-2}$ s $^{-1}$ ]	5.74	5.02
Observed Flux	(0.5-10 keV)	$10^{-11}$ [ergs cm $^{-2}$ s $^{-1}$ ]	0.289	0.137
Fit quality	C/dof			645.29/596
Blurred reflection	Neutral absorber ZPCFABS	nH ( $10^{22} \text{ cm}^{-2}$ )	$22 \pm 5$	$61 \pm 11$
		CF	$0.99 \pm 0.01$	$0.96^{+0.02}_{-0.01}$
	Intrinsic	$\Gamma$	$2.45^{+0.11}_{-0.14}$	$2.4 \pm 0.1$
	Power Law	norm ( $10^{-4}$ )	$< 22$	$< 18$
	FPMB Calibration	constant	$1.00 \pm 0.06$	
	Swift Calibration	constant	$1.0 \pm 0.2$	
	Collisionally Ionized material MEKAL	kT [keV]	-	$0.65 \pm 0.04$
		norm ( $10^{-5}$ ) [cm $^{-5}$ ]	-	$9 \pm 2$
		Metal Abundance [cosmic]	$1^f$	
	Distant Cold Reflector XILLVER	norm ( $10^{-5}$ )	-	$2.1 \pm 0.06$
		A <sub>Fe</sub> [solar]	$1^f$	
		$\log \xi$ [ergs cm s $^{-1}$ ]	$0^f$	
		E <sub>cut</sub> [keV]	$300^f$	
		Inclination [ $^\circ$ ]	$< 19^l$	
	Blurred reflector RELXILL	q <sub>in</sub>	$3^f$	
		q <sub>out</sub>	$3^f$	
		Break radius [r <sub>g</sub> ]	$6^f$	
		spin	$0.998^f$	
		Outer Radius [r <sub>g</sub> ]	$400^f$	
		Inclination [ $^\circ$ ]	-	$< 19$
		$\log \xi$ [ergs cm s $^{-1}$ ]	-	$3.00^{+0.07}_{-0.25}$
		A <sub>Fe</sub> [solar]	-	$4^{+2}_{-1}$
		E <sub>cut</sub> [keV]	$300^f$	
		norm ( $10^{-5}$ )	$10^{+6}_{-5}$	$4 \pm 1$
	(0.1-100 keV)	$10^{-11}$ [ergs cm $^{-2}$ s $^{-1}$ ]	9.85	4.32
	(0.5-10 keV)	$10^{-11}$ [ergs cm $^{-2}$ s $^{-1}$ ]	0.289	0.134
	C/dof			615.64/598
Unabsorbed Flux	(0.1-100 keV)	$10^{-11}$ [ergs cm $^{-2}$ s $^{-1}$ ]	9.85	4.32
Observed Flux	(0.5-10 keV)	$10^{-11}$ [ergs cm $^{-2}$ s $^{-1}$ ]	0.289	0.134
Fit quality	C/dof			615.64/598

**Table 3.** Best-fit model parameters for Mrk 1239. Column (1) indicated the tested model and column (2) indicates the model component. Column (3) gives the value of each parameter for the modern epoch. Column (4) gives the value for each parameter for the historic epoch. If a dash is present it indicated that the parameters are linked between epochs. All parameters with the superscript ‘f’ are kept fixed at quoted values. The parameters with superscript ‘l’ are linked between components. Normalizations with superscript ‘p’ are given by photons keV $^{-1}$  cm $^{-2}$  s $^{-1}$  at 1 keV.

parameter ( $\log \xi$ ) and the iron abundance ( $A_{\text{Fe}}$ ) are free to vary, but also linked between epochs.

We adopt very similar geometry as the partial covering model, where the very central region of the AGN is highly obscured, there is some amount of cold distant reflection and a star forming region at some large distance from the AGN. The XSPEC model used is  $\text{CONSTANT} \times \text{TBABS} \times (\text{MEKAL} + \text{XILLVER} + \text{ZPCFABS} \times (\text{RELXILL} + \text{POWERLAW}))$ . As in the partial covering model we test three scenarios: (i) constant continuum and varying absorbers; (ii) constant absorbers and vary continuum; and (iii) continuum and absorber parameters free to vary. Here, continuum refers to the power law and blurred reflection components together.

The initial model, with all parameters linked between epochs renders a very poor fit ( $C/\text{dof} = 1538.17/603$ ). Examining Test (i), if the CF was allowed to vary between epochs the fit statistic improves by  $\Delta C = 841.92$  for two additional free parameter. If instead  $N_{\text{H}}$  is allowed to vary between epochs and CF is linked, the improvement to the fit is  $\Delta C = 45.2$ . With both  $N_{\text{H}}$  and CF free between epochs the  $C/\text{dof} = 645.42/599$ .

In Test (ii), we linked absorbers and freed the continuum. If RELXILL normalization was free, but linked between epochs, the fit statistic is  $C/\text{dof} = 720.31/602$ . If instead the power law normalization was linked, but free to vary between epochs, there was no significant improvement in fit statistic. If both the RELXILL and power law normalization are allowed free to vary between epochs the fit statistic is  $C/\text{dof} = 679.53/601$ .

Test (iii) renders the best fit blurred reflection model. The parameters are given in Table 3. The best fit blurred reflection model gave a fit statistic of  $C/\text{dof} = 615.64/598$ . This was a marked improvement over linking the continuum or absorption parameters separately. The reflection fraction at each epoch was calculated by determining the unabsorbed flux contributions between 0.1 – 100 keV in the blurred reflector (RELXILL) and power law components. Error on the calculated reflection fraction are propagated from the uncertainties in the normalisation of each component. Only a lower limit could be calculated at both epochs, as only an upper limit could be placed on the power law flux. The reflection fraction for the *NuSTAR* epoch is  $> 2.5$ , for the MOS epoch  $> 1.3$ , so the model indicates the source is reflection dominated.

Only an upper limit could be measured for the inclination ( $< 19^\circ$ ) indicating the system is nearly face-on. Zhang & Wu (2002) measure an inclination of  $7^\circ$  from the broadline region, which is in good agreement with our measurement.

Figure 5 (top panel) shows the theoretical best fit blurred reflection model applied only to the FPMA data set for clarity. The intrinsic continuum is shown in cyan, the absorbed power law and blurred reflection component are shown in blue and green, respectively. This again shows the large

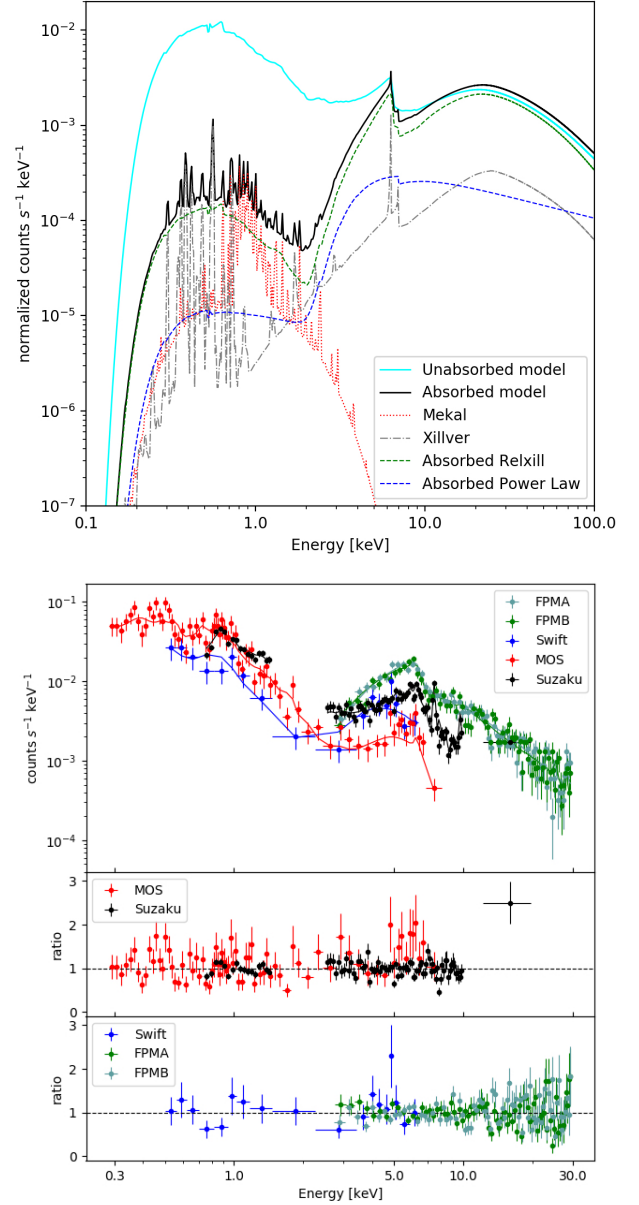


**Figure 5.** *Upper panel:* The theoretical best-fit blurred reflection model shown over the entire X-ray band. The cyan line shows the continuum power law and blurred reflector components with only Galactic absorption applied. This model appears to be reflection dominated. *Upper middle panel:* The folded spectra with the best fit blurred reflection model applied. *Lower middle panel:* The ratio of data to model for the historic epoch, which includes the MOS, XIS and PIN spectra. *Lower panel:* The ratio of data to model for the modern epoch, which contains the XRT and FPMA/FPMB spectra.

amount of absorption that is required for the MEKAL (red) component to be visible. As in the ionized partial covering model, we believe that the MEKAL is responsible for the 0.9 keV feature reported by Grupe et al. (2004). The torus emission is shown in gray and further contribute to the soft excess. The bottom three panels of Figure 5 show the data and residuals (separated by epoch) for the best fit blurred reflection model, the colours are the same as Figures 1 and 4. The fit has the same overall shape as the ionized partial cover model. We still see the residuals in the Fe K $\alpha$  band of the MOS spectra despite the fact that our model requires an over abundance of iron, which is commonly seen in NLS1. Over all the data fits well, and the soft band is again adequately described by the MEKAL component, and the long term variability is again driven by changes in the absorber.

## 5. DISCUSSION

The data of Mrk 1239 analysed in this work highlight distinct physical process that dominate above and below  $\sim 3$  keV. These two regimes feature dramatically different variability properties and physical origins. As such our discussion shall be divided into these two energy regimes. We interpret the spectra of Mrk 1239 to contain two distinct sources of emission, the first is the low energy star forming region and the second is the higher energy AGN component.

### 5.1. Origins of the soft excess

To begin, our analysis of the Suzaku data did not give any evidence for variability below 3 keV on short timescales. As well the unfolded spectra of Mrk 1239 showed a remarkable consistency over the 18 years of spectra coverage presented in this paper, with virtually no change in flux in the 0.3-3 keV while the harder band had significant change in flux over the same period. This is at odds with typical NLS1 where the soft band tends to have more variability (e.g. Leighly 1999). As well, the spectral features present in the soft band, like the strong emission line-like features observed by Grupe et al. (2004), are inconsistent with smooth spectra typically seen in NLS1s.

The long-term consistency of Mrk 1239 along with its unusual spectral shape lead us to apply different models to explain the soft excess. We use MEKAL to model the possible contribution from starburst activity that may be present in Mrk 1239 (Rodríguez-Ardila & Viegas 2003). This model has been used to describe many AGN that exhibit depressed power law emission from obscuration (e.g. Franceschini et al. 2003) or intrinsic variability like Mrk 335 (e.g. Gallo et al. 2019). In AGN dominated flux states, this component is still present, but overwhelmed by the AGN emission.

There is also a contribution to the line emission at low energies from the distant reflector (Figure 4 and 5). In combination, the MEKAL and XILLVER components nicely describe

the line-like features in the spectra without requiring additional Gaussian profiles or abnormal abundances. We considered the possibility that the emission could be due entirely to photoionized gas, perhaps from the narrow-line region. We tested this by replacing MEKAL with a PHOTEMIS component to our best fit ionized partial covering model for just the MOS spectra between 0.3 – 2 keV. The model was only applied to the MOS spectra as it is computationally intensive. If there were any improvements over MEKAL, they would be most obvious in the the MOS spectra. The best fit PHOTEMIS model resulted in a poorer fit than with MEKAL ( $\Delta C = 30$ ) for the same number of free parameter, and positive residuals in the 0.8 – 1 keV band remained.

Table 4 show the flux and luminosity for each component between 0.5 – 2 keV at each epoch. We can see that the MEKAL component has a consistently strong contribution in both models with the central engine absorbed. But when the central engine absorption is removed, the line-emission MEKAL is completely overwhelmed by the power law contribution in the partial covering scenario and by the power law and RELXILL contribution in the blurred reflection scenario.

We are using MEKAL to describe the X-ray evidence of a starburst activity. Mrk 1239 has significant evidence of star burst activity. The PAH signatures found by Rodríguez-Ardila & Viegas (2003) agrees with this interpretation. The starburst regions are included in the X-ray extraction regions of the instruments used due to the modest angular resolution.

A study of ten ultraluminous infrared galaxies (ULIRGs) by Franceschini et al. (2003) used MEKAL to model the SFR in selected galaxies. They measured the average temperature of the MEKAL component to be  $kT \approx 0.7$  keV which agrees exactly with the temperature measured in Mrk 1239 ( $kT \approx 0.66$  keV). The luminosity we measure for the MEKAL component also agrees with the luminosity Franceschini et al. (2003) measured in their sample.

Franceschini et al. (2003) also give a method to approximate the SFR using  $L_{2-10 \text{ keV}}$ :

$$\text{SFR}_{\text{X-ray}}^{\text{ULIRG}} \approx \frac{L_{2-10 \text{ keV}}}{10^{39} \text{ erg s}^{-1}} M_{\odot} \text{ yr}^{-1} \quad (1)$$

If we measure the  $L_{2-10 \text{ keV}}$  for just the unabsorbed MEKAL component we get a SFR of 5.8 and 3.7  $M_{\odot} \text{ yr}^{-1}$  based on the ionized partial cover and blurred reflection model respectively. This agrees nicely with the SFR predicted by the PAH signatures (Ruschel-Dutra et al. 2016).

Another interesting feature of MEKAL component is that it appears to be independent of the continuum model tested. The MEKAL temperature and normalization agree with each other to within 1 and  $2\sigma$ , respectively. This suggests that regardless of the mechanism producing the observed curvature at high energies, the soft X-ray emission of Mrk 1239 can be nicely explained by the starburst component and some photoionised emission from distant emission, without the need



(1)	(2)	(3)	(4)	(5)	(6)	(7)
Model	Instrument	Component	Absorbed Flux [ergs cm <sup>-2</sup> s <sup>-1</sup> ]	Absorbed Luminosity [ergs s <sup>-1</sup> ]	Unabsorbed Flux [ergs cm <sup>-2</sup> s <sup>-1</sup> ]	Unabsorbed Luminosity [ergs s <sup>-1</sup> ]
Blurred Reflection	<i>Swift/NuSTAR</i>	Power Law	$2.20 \times 10^{-14}$	$1.98 \times 10^{40}$	$1.88 \times 10^{-12}$	$1.71 \times 10^{42}$
		Relxill	$17.0 \times 10^{-14}$	$15.6 \times 10^{40}$	$1.52 \times 10^{-11}$	$1.40 \times 10^{43}$
		Xillver	$7.39 \times 10^{-14}$	$6.73 \times 10^{40}$	$9.36 \times 10^{-14}$	$8.55 \times 10^{40}$
		Mekal	$11.6 \times 10^{-14}$	$10.5 \times 10^{40}$	$1.30 \times 10^{-13}$	$1.17 \times 10^{41}$
	<i>MOS/Suzaku</i>	Power Law	$6.13 \times 10^{-14}$	$5.53 \times 10^{40}$	$1.85 \times 10^{-12}$	$1.67 \times 10^{42}$
		Relxill	$19.6 \times 10^{-14}$	$18.0 \times 10^{40}$	$6.13 \times 10^{-12}$	$5.64 \times 10^{42}$
		Xillver	$7.18 \times 10^{-14}$	$6.48 \times 10^{40}$	$9.10 \times 10^{-14}$	$8.23 \times 10^{40}$
		Mekal	$11.6 \times 10^{-14}$	$10.5 \times 10^{40}$	$1.30 \times 10^{-13}$	$1.18 \times 10^{41}$
Partial Covering	<i>Swift/NuSTAR</i>	Power Law	$16.1 \times 10^{-14}$	$14.9 \times 10^{40}$	$1.38 \times 10^{-11}$	$1.25 \times 10^{43}$
		Xillver	$4.97 \times 10^{-14}$	$45.1 \times 10^{40}$	$6.25 \times 10^{-14}$	$5.70 \times 10^{40}$
		Mekal	$17.0 \times 10^{-14}$	$15.3 \times 10^{40}$	$1.90 \times 10^{-13}$	$1.71 \times 10^{41}$
	<i>MOS/Suzaku</i>	Power Law	$22.5 \times 10^{-14}$	$20.6 \times 10^{40}$	$1.21 \times 10^{-11}$	$1.09 \times 10^{43}$
		Xillver	$4.86 \times 10^{-14}$	$43.8 \times 10^{40}$	$6.12 \times 10^{-14}$	$5.53 \times 10^{40}$
		Mekal	$17.0 \times 10^{-14}$	$15.3 \times 10^{40}$	$1.90 \times 10^{-13}$	$1.72 \times 10^{41}$

**Table 4.** Flux and luminosity for each model component between 0.5 – 2 keV. Column (1) indicates the model used for the measurements. Columns (2) and (3) denotes the instrument used/the epoch and the model component measured respectively. Columns (4) and (5) list the absorbed flux and luminosity between 0.5 – 2 keV. Columns (6) and (7) list the unabsorbed flux and luminosity between 0.5 – 2 keV. There are small discrepancies in the flux and luminosity measured between epochs in the same model even though the xillver component are shared between epochs. This is due to the differences in telescope responses.

for significant overabundances of Ne or other elements. We found that the spectral feature [Grupe et al. \(2004\)](#) reported as a Ne overabundance was a blend of many Fe L transitions.

We found that the spectral feature [Grupe et al. \(2004\)](#) reported as a Ne overabundance was a blend of many Fe L transitions. We examined if adopting different cosmic abundances in XSPEC could alter the fit quality. Regardless, of the abundance table used, the MEKAL temperature remained between 0.63 – 0.65 keV and the fit quality was  $C = 162 - 167$  for 165 dof.

### 5.2. The hard X-ray spectrum of Mrk 1239

The light curves seen in Figure 2 show rapid variability between 3 – 10 keV. Similarly, the multi-epoch spectra in Figure 1 suggest long term variability between 3 – 10 keV. In Section 3.2, the excess variance in the *NuSTAR* light curve was calculated and determined to be  $\sigma_{\text{rms}}^2 = 0.04 \pm 0.01$ . With the caveats that our analysis uses slightly different energy bands and time bins, the measured value of  $\sigma_{\text{rms}}^2$  for Mrk 1239 is comparable to the average value [Ponti et al.](#)

(2012) measured for NLS1s ( $\sigma_{\text{NLS1}}^2 \approx 0.02$ ). Following the  $M_{\text{BH}}-\sigma_{\text{rms}}$  relation found by [Ponti et al. \(2012\)](#), we estimate a black hole mass of  $2 \times 10^6 M_{\odot}$  for Mrk 1239, which is in agreement with other works (see [Ryan et al. 2007](#)). Based on the rapid variability in the 3 – 10 keV band, Mrk 1239 behaves like an unobscured NLS1. The central black hole region is exposed in the 3 – 10 keV band.

Independent of the scenarios tested (i.e. partial covering or blurred reflection), the photon index of the intrinsic power law component is comparable ( $\Gamma \sim 2.3$ ). The measured value is much flatter than has been measured in other works ([Grupe et al. 2004](#)), but it is more consistent with what is expected from Seyfert galaxies and NLS1s ([Grupe et al. 2010](#)). Estimating the Eddington luminosity ratio from  $\Gamma$  based on the relationship in [Brightman et al. \(2013\)](#) gives  $L/L_{\text{Edd}} \sim 1 - 1.5$  for Mrk 1239. This is consistent with the value estimated by [Yao et al. \(2018\)](#). The high value implies a rapid accretor, which is also characteristic of the NLS1 class. Alternatively, the value could be overestimated if the primary

emission is anisotropic, which might be consistent with the jet interpretation for some of the radio emission (Doi et al. 2015).

Comparing the partial covering and blurred reflection scenarios directly, similar neutral absorbers that are responsible for obscuring the low energy X-rays and revealing the starburst regions are required in both models. In both models the column density decreases between the historic and modern epochs. The main difference in the two scenarios is the strength of the primary power law. In the blurred reflection scenario the spectra is extremely reflection dominated with the reflection fraction  $> 1.3$  and  $> 2.5$  for the historic and modern epoch, respectively. The reflection dominated interpretation may be at odds with the value of the emissivity index being fixed to  $q_{\text{in}} = 3$  (allowing it to be free did not improve the fit), which would imply an inner disk that is truncated at a large radius or a corona that is very high above the disc. A high reflection fraction requires a significant amount of light bending or a non-standard geometry for the accretion disc.

Though it appears clear that we are observing emission originating close to the black hole, it is difficult to produce a self-consistent blurred reflection model with the current data. The ionized partial covering scenario has the advantage of being consistent with the high levels of polarization seen in the optical band by Martin et al. (1983) and Goodrich (1989).

In both of the scenarios, the primary emission variability is minimal on long timescales. The change in flux above 3 keV observed on long timescales is driven by the absorbers. A possible explanation for the large amount of absorbing material surrounding the AGN could be that it contains a Schwarzschild black hole. According to Ishibashi (2020), non-spinning black holes have less radiation pressure to drive obscuring gas and dust out of our line of sight than Kerr black holes do. The best fit blurred reflection model with  $a = 0$  results in a fit of  $C/\text{dof} = 625.50/598$ . Most fit parameters remained similar to the values we report in Table 3, except for the iron abundance which decreases to  $A_{\text{Fe}} = 2.2$ . Although the fit is not as good as that produced by the Kerr black hole model, a non-spinning black hole is more consistent with the low emissivity profile that is adopted.

Figure 6 show a diagram for the physical scenario we propose. The top box shows the physical scenario for the ionized partial covering model. Here photons are emitted by the disc in the UV and are Compton-upscattered by the corona. The primary X-ray photons are then emitted by the corona, where they encounter the partial covering components. This includes a neutral partial cover and an ionized partial cover (warm absorber). In our model most of the photons interact with the absorbers, and few escape the inner region unaffected. This is due to the high CF we measure. The bottom of the two boxes show the AGN for the blurred reflection sce-

nario. Here UV photons are produced by the disc, Compton-upscattered by the corona and then reflected off of the disc. Both the primary and blurred reflected emission are absorbed by a neutral absorber before leaving the AGN. Once we move out to the torus our diagrams for the ionized partial cover and blurred reflection scenario are the same. The photons from the AGN interact with the torus to give us cold distant reflection emission lines. Then our collisionally ionized material, which we believe is starburst activity and therefore must be located within 400 pc of the central engine as PAH measurements show starburst activity here (Ruschel-Dutra et al. 2016). Outside of the starburst region we see no evidence of further emission in the X-ray band. Alternatively the cold absorber could be associated with the torus. Perhaps our line-of-sight is grazing the torus or the torus is more patchy and isotropic around the primary source.

The difference in each of these scenarios is how the primary continuum is produced and then absorbed. If the absorbing material is in fact surrounding the AGN then it stands to reason that the absorbing material is what is driving the long term variability in Mrk 1239. This is the case regardless of which model (ionised partial covering or blurred reflection) is implied as the additional component to fit the continuum above 3 keV.

## 6. CONCLUSION

In this work, multi-epoch X-ray spectra spanning 18 years of the NLS1 galaxy Mrk 1239 are presented. This study combines data from *XMM-Newton* and *Suzaku* with a simultaneous *NuSTAR* and *Swift* observation to study the spectrum and variability of this source. A comparison of the unfolded spectra reveals that the spectra are very similar at all epochs below 3 keV, while the *NuSTAR* and *Swift* data are brighter by a factor of 2 – 3 at higher energies. The light curves also reveal no short term variability below 3 keV, while modest variability at higher energies is seen.

Motivated by this, and by signatures of star formation in the infrared spectra presented in previous works, we successfully model the soft spectrum with emission from a hot plasma. When the absorption component is removed, the starburst component accounts for  $\sim 1 - 10$  per cent of the total emission, which is sensible for a type-1 AGN. Both a blurred reflection and ionised partial covering model are employed to explain the remainder of the emission. Both models have several key components in common; a power law component with a slope of  $\sim 2.3 - 2.4$ , a neutral absorber with a covering fraction near  $\sim 1$ , and contributions from a distant reflector (e.g. the torus). There are some apparent inconsistencies which may be difficult to explain in the blurred reflection model, including a high iron abundance, and a low emissivity index despite having a reflection dominated spectrum. By contrast, the two-component absorption model may

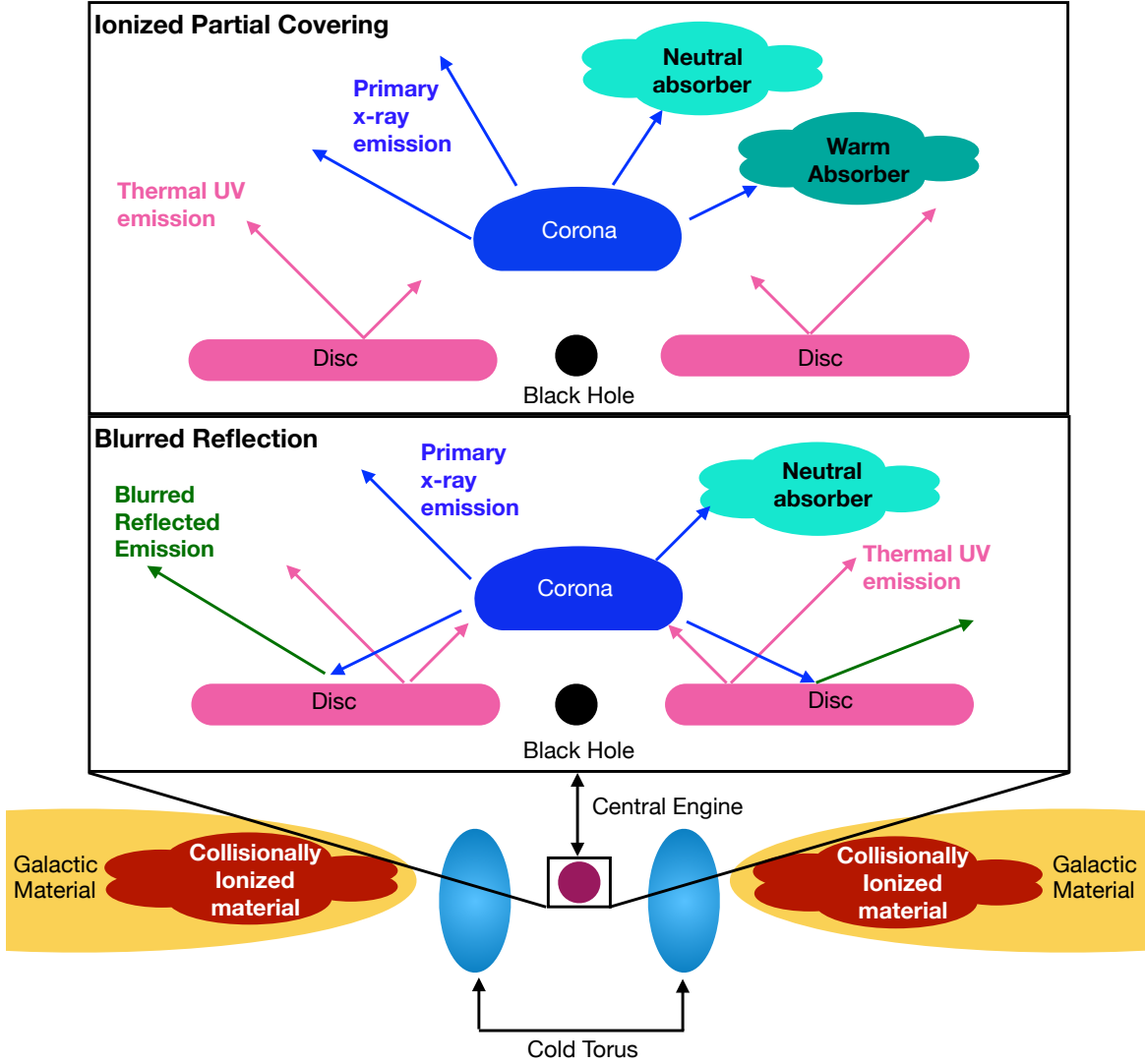


**Figure 6.** A graphic interpretation of our proposed models. The top box shows the AGN in the ionized partial covering scenario. The bottom box show the AGN in the blurred reflection scenario. In both the ionized partial covering and blurred reflection scenarios, the absorption of the primary continuum is inside the torus.

agree with the two polarisation regions found in the optical emission.

Deep observations with calorimeter-type resolution (e.g. Takahashi et al. 2016) such as *XRISM* (Tashiro et al. 2018) may help to reveal any emission line features present in the low energy spectrum from the starburst and distant reflection components. They may also reveal absorption features present at high energies, helping to confirm the high level of absorption required to fit the observed curvature. Additionally, future observations with *XMM-Newton* may help to confirm the minimal level of low energy variability and support a starburst emission component to explain the soft emission from this unique source.

#### ACKNOWLEDGEMENTS

Many thanks to Adam Gonzalez for insightful discussions. The authors thank the anonymous referee for their comments. The *XMM-Newton* project is an ESA Science Mission with instruments and contributions directly funded by ESA Member States and the USA (NASA). This research has made use of data obtained from the *Suzaku* satellite, a collaborative mission between the space agencies of Japan (JAXA) and the USA (NASA). Additionally, this work made use of data supplied by the UK Swift Science Data Centre at the University of Leicester, data from the NuSTAR mission, a project led by the California Institute of Technology, managed by the Jet Propulsion Laboratory, and funded by the National Aeronau-

tics and Space Administration. MZB, SGHW and LCG acknowledge the support of the Natural Sciences and Engineering Research Council of Canada (NSERC). LCG acknowl-

edges financial support from the Canadian Space Agency (CSA).

## REFERENCES

- Antonucci, R. 1993, *ARAA*, 31, 473,  
doi: [10.1146/annurev.aa.31.090193.002353](https://doi.org/10.1146/annurev.aa.31.090193.002353)
- Ballantyne, D. R., Ross, R. R., & Fabian, A. C. 2001, *MNRAS*, 327, 10, doi: [10.1046/j.1365-8711.2001.04432.x](https://doi.org/10.1046/j.1365-8711.2001.04432.x)
- Beers, T. C., Kriessler, J. R., Bird, C. M., & Huchra, J. P. 1995, *AJ*, 109, 874, doi: [10.1086/117329](https://doi.org/10.1086/117329)
- Berton, M., Congiu, E., Järvelä, E., et al. 2018, *A&A*, 614, A87,  
doi: [10.1051/0004-6361/201832612](https://doi.org/10.1051/0004-6361/201832612)
- Boller, T., Brandt, W. N., & Fink, H. 1996, *AAP*, 305, 53,  
<https://arxiv.org/abs/astro-ph/9504093>
- Boller, T., Fabian, A., Sunyaev, R., et al. 2002, *Monthly Notices of the Royal Astronomical Society*, 329, L1,  
doi: [10.1046/j.1365-8711.2002.05040.x](https://doi.org/10.1046/j.1365-8711.2002.05040.x)
- Bonson, K., & Gallo, L. C. 2016, *MNRAS*, 458, 1927,  
doi: [10.1093/mnras/stw466](https://doi.org/10.1093/mnras/stw466)
- Bonson, K., Gallo, L. C., Wilkins, D. R., & Fabian, A. C. 2018, *Monthly Notices of the Royal Astronomical Society*, 477, 3247,  
doi: [10.1093/mnras/sty828](https://doi.org/10.1093/mnras/sty828)
- Boorman, P. G., Gandhi, P., Stern, D., Harrison, F., & NuSTAR Obscured AGN Team. 2018, in *American Astronomical Society Meeting Abstracts*, Vol. 231, American Astronomical Society Meeting Abstracts #231, 343.01
- Brightman, M., Silverman, J. D., Mainieri, V., et al. 2013, *Monthly Notices of the Royal Astronomical Society*, 433, 2485,  
doi: [10.1093/mnras/stt920](https://doi.org/10.1093/mnras/stt920)
- Cash, W. 1979, *ApJ*, 228, 939, doi: [10.1086/156922](https://doi.org/10.1086/156922)
- Chiang, C.-Y., Walton, D. J., Fabian, A. C., Wilkins, D. R., & Gallo, L. C. 2015, *MNRAS*, 446, 759,  
doi: [10.1093/mnras/stu2087](https://doi.org/10.1093/mnras/stu2087)
- Doi, A., Wajima, K., Hagiwara, Y., & Inoue, M. 2015, *ApJL*, 798, L30, doi: [10.1088/2041-8205/798/2/L30](https://doi.org/10.1088/2041-8205/798/2/L30)
- Evans, P. A., Beardmore, A. P., Page, K. L., et al. 2009, *Monthly Notices of the Royal Astronomical Society*, 397, 1177,  
doi: [10.1111/j.1365-2966.2009.14913.x](https://doi.org/10.1111/j.1365-2966.2009.14913.x)
- Fabian, A. C., Miniutti, G., Gallo, L., et al. 2004, *MNRAS*, 353, 1071, doi: [10.1111/j.1365-2966.2004.08036.x](https://doi.org/10.1111/j.1365-2966.2004.08036.x)
- Fabian, A. C., Zoghbi, A., Ross, R. R., et al. 2009, *Nature*, 459, 540, doi: [10.1038/nature08007](https://doi.org/10.1038/nature08007)
- Fanaroff, B. L., & Riley, J. M. 1974, *MNRAS*, 167, 31P,  
doi: [10.1093/mnras/167.1.31P](https://doi.org/10.1093/mnras/167.1.31P)
- Franceschini, A., Braito, V., Persic, M., et al. 2003, *MNRAS*, 343, 1181, doi: [10.1046/j.1365-8711.2003.06744.x](https://doi.org/10.1046/j.1365-8711.2003.06744.x)
- Fukazawa, Y., Mizuno, T., Watanabe, S., et al. 2009, *PASJ*, 61, S17, doi: [10.1093/pasj/61.sp1.S17](https://doi.org/10.1093/pasj/61.sp1.S17)
- Gallo, L. 2018, *Proceedings of Revisiting narrow-line Seyfert 1 galaxies and their place in the Universe PoS(NLS1-2018)*,  
doi: [10.22323/1.328.0034](https://doi.org/10.22323/1.328.0034)
- Gallo, L. C., Fabian, A. C., Grupe, D., et al. 2012, *Monthly Notices of the Royal Astronomical Society*, 428, 1191,  
doi: [10.1093/mnras/sts102](https://doi.org/10.1093/mnras/sts102)
- Gallo, L. C., Wilkins, D. R., Bonson, K., et al. 2015, *Monthly Notices of the Royal Astronomical Society*, 446, 633,  
doi: [10.1093/mnras/stu2108](https://doi.org/10.1093/mnras/stu2108)
- Gallo, L. C., Gonzalez, A. G., Waddell, S. G. H., et al. 2019, *MNRAS*, 484, 4287, doi: [10.1093/mnras/stz274](https://doi.org/10.1093/mnras/stz274)
- García, J., Dauser, T., Lohfink, A., et al. 2014, *ApJ*, 782, 76,  
doi: [10.1088/0004-637X/782/2/76](https://doi.org/10.1088/0004-637X/782/2/76)
- Goodrich, R. W. 1989, *ApJ*, 342, 224, doi: [10.1086/167586](https://doi.org/10.1086/167586)
- Grupe, D., Beuermann, K., Thomas, H. C., Mannheim, K., & Fink, H. H. 1998, *A&A*, 330, 25,  
<https://arxiv.org/abs/astro-ph/9710298>
- Grupe, D., Komossa, S., Leighly, K. M., & Page, K. L. 2010, *ApJS*, 187, 64, doi: [10.1088/0067-0049/187/1/64](https://doi.org/10.1088/0067-0049/187/1/64)
- Grupe, D., Mathur, S., & Komossa, S. 2004, *The Astronomical Journal*, 127, 3161, doi: [10.1086/421002](https://doi.org/10.1086/421002)
- Grupe, D., Thomas, H. C., & Beuermann, K. 2001, *A&A*, 367, 470, doi: [10.1051/0004-6361:20000429](https://doi.org/10.1051/0004-6361:20000429)
- Grupe, D., Komossa, S., Gallo, L., et al. 2019, *Monthly Notices of the Royal Astronomical Society*, 486, 227,  
doi: [10.1093/mnras/stz819](https://doi.org/10.1093/mnras/stz819)
- Harrison, F. A., Craig, W. W., Christensen, F. E., et al. 2013, *ApJ*, 770, 103, doi: [10.1088/0004-637X/770/2/103](https://doi.org/10.1088/0004-637X/770/2/103)
- Holt, S. S., Mushotzky, R. F., Becker, R. H., et al. 1980, *ApJL*, 241, L13, doi: [10.1086/183350](https://doi.org/10.1086/183350)
- Ishibashi, W. 2020, *Monthly Notices of the Royal Astronomical Society*, 495, 2515, doi: [10.1093/mnras/staa1382](https://doi.org/10.1093/mnras/staa1382)
- Iso, N., Ebisawa, K., Sameshima, H., et al. 2016, *Publications of the Astronomical Society of Japan*, 68,  
doi: [10.1093/pasj/psw015](https://doi.org/10.1093/pasj/psw015)
- Jansen, F., Lumb, D., Altieri, B., et al. 2001, *AAP*, 365, L1,  
doi: [10.1051/0004-6361:20000036](https://doi.org/10.1051/0004-6361:20000036)
- Jensen, J. J., Hönig, S. F., Rakshit, S., et al. 2017, *MNRAS*, 470, 3071, doi: [10.1093/mnras/stx1447](https://doi.org/10.1093/mnras/stx1447)
- Jiang, J., Fabian, A. C., Dauser, T., et al. 2019, *MNRAS*, 489, 3436, doi: [10.1093/mnras/stz2326](https://doi.org/10.1093/mnras/stz2326)
- Kaastra, J. S., & Bleeker, J. A. M. 2016, *A&A*, 587, A151,  
doi: [10.1051/0004-6361/201527395](https://doi.org/10.1051/0004-6361/201527395)



- Komossa, S. 2008, in *Revista Mexicana de Astronomia y Astrofisica Conference Series*, Vol. 32, *Revista Mexicana de Astronomia y Astrofisica Conference Series*, 86–92, <https://arxiv.org/abs/0710.3326>
- Komossa, S., Grupe, D., Schartel, N., et al. 2016, *Proceedings of the International Astronomical Union*, 12, 168171, doi: [10.1017/S1743921317001648](https://doi.org/10.1017/S1743921317001648)
- Leighly, K. M. 1999, *ApJs*, 125, 317, doi: [10.1086/313287](https://doi.org/10.1086/313287)
- Liedahl, D. A., Osterheld, A. L., & Goldstein, W. H. 1995, *ApJL*, 438, L115, doi: [10.1086/187729](https://doi.org/10.1086/187729)
- Marin, F. 2016, *Monthly Notices of the Royal Astronomical Society*, 460, 3679, doi: [10.1093/mnras/stw1131](https://doi.org/10.1093/mnras/stw1131)
- Martin, P. G., Thompson, I. B., Maza, J., & Angel, J. R. P. 1983, *ApJ*, 266, 470, doi: [10.1086/160795](https://doi.org/10.1086/160795)
- Miniutti, G., & Fabian, A. C. 2004, *Monthly Notices of the Royal Astronomical Society*, 349, 1435, doi: [10.1111/j.1365-2966.2004.07611.x](https://doi.org/10.1111/j.1365-2966.2004.07611.x)
- Mitsuda, K., Bautz, M., Inoue, H., et al. 2007, *PASJ*, 59, S1, doi: [10.1093/pasj/59.sp1.S1](https://doi.org/10.1093/pasj/59.sp1.S1)
- Miyakawa, T., Ebisawa, K., & Inoue, H. 2012, *PASJ*, 64, 140, doi: [10.1093/pasj/64.6.140](https://doi.org/10.1093/pasj/64.6.140)
- Nandra, K., O’Neill, P. M., George, I. M., & Reeves, J. N. 2007, *Monthly Notices of the Royal Astronomical Society*, 382, 194, doi: [10.1111/j.1365-2966.2007.12331.x](https://doi.org/10.1111/j.1365-2966.2007.12331.x)
- Nikolajuk, M., Czerny, B., & Gurynowicz, P. 2009, *Monthly Notices of the Royal Astronomical Society*, 394, 2141, doi: [10.1111/j.1365-2966.2009.14478.x](https://doi.org/10.1111/j.1365-2966.2009.14478.x)
- Osterbrock, D. E., & Pogge, R. W. 1985, *ApJ*, 297, 166, doi: [10.1086/163513](https://doi.org/10.1086/163513)
- Parker, M. L., Longinotti, A. L., Schartel, N., et al. 2019, *Monthly Notices of the Royal Astronomical Society*, 490, 683, doi: [10.1093/mnras/stz2566](https://doi.org/10.1093/mnras/stz2566)
- Ponti, G., Papadakis, I., Bianchi, S., et al. 2012, *A&A*, 542, A83, doi: [10.1051/0004-6361/201118326](https://doi.org/10.1051/0004-6361/201118326)
- Ponti, G., Gallo, L. C., Fabian, A. C., et al. 2010, *MNRAS*, 406, 2591, doi: [10.1111/j.1365-2966.2010.16852.x](https://doi.org/10.1111/j.1365-2966.2010.16852.x)
- Pounds, K. A., Done, C., & Osborne, J. P. 1995, *MNRAS*, 277, L5, doi: [10.1093/mnras/277.1.L5](https://doi.org/10.1093/mnras/277.1.L5)
- Puchnarewicz, E. M., Mason, K. O., Cordova, F. A., et al. 1992, *MNRAS*, 256, 589, doi: [10.1093/mnras/256.3.589](https://doi.org/10.1093/mnras/256.3.589)
- Reeves, J., Done, C., Pounds, K., et al. 2008, *Monthly Notices of the Royal Astronomical Society: Letters*, 385, L108, doi: [10.1111/j.1745-3933.2008.00443.x](https://doi.org/10.1111/j.1745-3933.2008.00443.x)
- Rodríguez-Ardila, A., & Mazzalay, X. 2006, *Monthly Notices of the Royal Astronomical Society: Letters*, 367, L57, doi: [10.1111/j.1745-3933.2006.00139.x](https://doi.org/10.1111/j.1745-3933.2006.00139.x)
- Rodríguez-Ardila, A., & Viegas, S. M. 2003, *MNRAS*, 340, L33, doi: [10.1046/j.1365-8711.2003.06538.x](https://doi.org/10.1046/j.1365-8711.2003.06538.x)
- Ross, R. R., & Fabian, A. C. 2005, *Monthly Notices of the Royal Astronomical Society*, 358, 211, doi: [10.1111/j.1365-2966.2005.08797.x](https://doi.org/10.1111/j.1365-2966.2005.08797.x)
- Ruschel-Dutra, D., Rodríguez Espinosa, J. M., González Martn, O., Pastoriza, M., & Riffel, R. 2016, *Monthly Notices of the Royal Astronomical Society*, 466, 3353, doi: [10.1093/mnras/stw3276](https://doi.org/10.1093/mnras/stw3276)
- Rush, B., & Malkan, M. A. 1996, *ApJ*, 456, 466, doi: [10.1086/176672](https://doi.org/10.1086/176672)
- Ryan, C. J., De Robertis, M. M., Virani, S., Laor, A., & Dawson, P. C. 2007, *ApJ*, 654, 799, doi: [10.1086/509313](https://doi.org/10.1086/509313)
- Sani, E., Lutz, D., Risaliti, G., et al. 2010, *Monthly Notices of the Royal Astronomical Society*, 403, 1246, doi: [10.1111/j.1365-2966.2009.16217.x](https://doi.org/10.1111/j.1365-2966.2009.16217.x)
- Takahashi, T., Kokubun, M., Mitsuda, K., et al. 2016, in *Society of Photo-Optical Instrumentation Engineers (SPIE) Conference Series*, Vol. 9905, *Proc. SPIE*, 99050U, doi: [10.1117/12.2232379](https://doi.org/10.1117/12.2232379)
- Tanaka, Y., Boller, T., & Gallo, L. 2005, in *Growing Black Holes: Accretion in a Cosmological Context*, ed. A. Merloni, S. Nayakshin, & R. A. Sunyaev, 290–295, doi: [10.1007/11403913\\_52](https://doi.org/10.1007/11403913_52)
- Tanaka, Y., Boller, T., Gallo, L., Keil, R., & Ueda, Y. 2004, *Publications of the Astronomical Society of Japan*, 56, L9, doi: [10.1093/pasj/56.3.L9](https://doi.org/10.1093/pasj/56.3.L9)
- Tanaka, Y., Ueda, Y., & Boller, T. 2003, *Monthly Notices of the Royal Astronomical Society*, 338, L1, doi: [10.1046/j.1365-8711.2003.06110.x](https://doi.org/10.1046/j.1365-8711.2003.06110.x)
- Tashiro, M., Maejima, H., Toda, K., et al. 2018, in *Society of Photo-Optical Instrumentation Engineers (SPIE) Conference Series*, Vol. 10699, *Proc. SPIE*, 1069922, doi: [10.1117/12.2309455](https://doi.org/10.1117/12.2309455)
- Truemper, J. 1982, *Advances in Space Research*, 2, 241, doi: [10.1016/0273-1177\(82\)90070-9](https://doi.org/10.1016/0273-1177(82)90070-9)
- Turner, T. J., Miller, L., Reeves, J. N., & Kraemer, S. B. 2007, *A&A*, 475, 121, doi: [10.1051/0004-6361:20077947](https://doi.org/10.1051/0004-6361:20077947)
- Véron-Cetty, M. P., & Véron, P. 2001, *AAP*, 374, 92, doi: [10.1051/0004-6361:20010718](https://doi.org/10.1051/0004-6361:20010718)
- Waddell, S. G. H., Gallo, L. C., Gonzalez, A. G., Tripathi, S., & Zoghbi, A. 2019, *MNRAS*, 489, 5398, doi: [10.1093/mnras/stz2518](https://doi.org/10.1093/mnras/stz2518)
- Walton, D. J., Nardini, E., Gallo, L. C., et al. 2019, *MNRAS*, 484, 2544, doi: [10.1093/mnras/stz115](https://doi.org/10.1093/mnras/stz115)
- Willingale, R., Starling, R. L. C., Beardmore, A. P., Tanvir, N. R., & O’Brien, P. T. 2013, *MNRAS*, 431, 394, doi: [10.1093/mnras/stt175](https://doi.org/10.1093/mnras/stt175)
- Wilms, J., Allen, A., & McCray, R. 2000, *ApJ*, 542, 914, doi: [10.1086/317016](https://doi.org/10.1086/317016)
- Yao, S., Qiao, E., Wu, X.-B., & You, B. 2018, *MNRAS*, 477, 1356, doi: [10.1093/mnras/sty788](https://doi.org/10.1093/mnras/sty788)
- Zhang, T.-Z., & Wu, X.-B. 2002, *ChJA&A*, 2, 487, doi: [10.1088/1009-9271/2/6/487](https://doi.org/10.1088/1009-9271/2/6/487)